

Direct low-energy trajectories to Near-Earth Objects

E. Fantino^{*a}, R. Flores^a, G. Donnarumma^{a,b}, D. Canales^c, K. C. Howell^d

^a*Department of Aerospace Engineering, Khalifa University of Science and Technology, P.O. Box 127788, Abu Dhabi (United Arab Emirates)*

^b*Department of Industrial Engineering, University of Naples Federico II, Piazzale Tecchio 80, 80125, Naples (Italy)*

^c*Department of Aerospace Engineering, Embry–Riddle Aeronautical University, Daytona Beach, FL 32117 (USA)*

^d*School of Aeronautics and Astronautics, Purdue University, West Lafayette, IN 47907 (USA)*

Abstract

Near-Earth Objects (NEOs) are asteroids, comets and meteoroids in heliocentric orbits with perihelion below 1.3 au. Similarly to the population of the Main Asteroid Belt, NEOs are primordial bodies and their study can improve our understanding of the origins of the Solar System. With a catalog of over 30 000 known asteroids and approximately 100 listed short-period comets, the NEO population represents an inventory of exploration targets reachable with significantly lower cost than the objects of the Main Asteroid Belt. In addition, the materials present in these bodies could be used to resupply spacecraft en route to other destinations. The trajectories of past missions to NEOs have been designed with the patched-conics technique supplemented by impulsive and/or low-thrust maneuvers and planetary gravity assist. The transfer times range from some months to a few years, and the close-approach speeds relative to the target have been as high as 10 km/s. The design technique described in this work leverages the invariant structures of the circular restricted three-body problem (CR3BP) to connect the vicinity of the Earth with NEOs in low-eccentricity, low-inclination orbits. The fundamental building blocks are periodic orbits around the collinear points L_1 and L_2 of the Sun-Earth CR3BP. These orbits are used to generate paths that follow the associated hyperbolic

^{*}Corresponding author: elena.fantino@ku.ac.ae (E. Fantino)

invariant manifolds, exit the sphere of influence of the Earth and reach NEOs on nearby orbits. The strategy is simple, can be applied to depart either a libration point orbit or the vicinity of the Earth, and offers attractive performance features.

Keywords: Circular restricted three-body problem, Hyperbolic invariant manifolds, Two-body problem, Near-Earth Objects, Rendezvous, Impulsive maneuvers

1. Introduction

Near-Earth Objects (NEOs) are asteroids (NEAs) and comets (NECs) with perihelion below 1.3 au [1]. Aphelia of NEAs generally lie within a sphere of radius 5.2 au, defined by Jupiter's orbit. Only short-period comets (i.e., orbital period less than 200 years) are considered NECs [2]. Scientists believe that the characterization of these objects is key to deepening our understanding of the origin and evolution of the Solar System, and the source of water on Earth. These bodies have also received attention because of their proximity to Earth, which is often associated with collision threats [3, 4]. Lastly, in recent years, NEOs have gained importance in the context of resource utilization, as *in-situ* collection and storage of material available in space could reduce the cost of space missions [5].

The first spacecraft (S/C) to visit a NEO was NASA's NEAR Shoemaker which landed on the surface of 433 Eros in 2001 [6]. This endeavour was followed by NASA's Deep Impact mission to comet Tempel 1 in 2005 [7]. The same year, JAXA's Hayabusa probe collected samples from asteroid Itokawa and delivered them to Earth in 2010 [8]. Also in 2010, Deep Impact's mission extension (EPOXI) carried out a flyby with comet Hartley 2 [9]. In 2012, CNSA's Change'e 2 executed a close approach with 4179 Toutatis [10]. Between 2018 and 2020, JAXA's follow-up mission Hayabusa 2 rendezvoused with asteroid Ryugu, collected samples of its surface and returned them to Earth [11]. The S/C is now on an extended mission to asteroid 1998 KY26. NASA's OSIRIS-

Rex successfully rendezvoused with Bennu, touched down on its surface in 2020 and extracted samples that were delivered to Earth in 2023 [12, 13]. The probe is continuing its journey to encounter and study 99942 Apophis in 2029. The Double Asteroid Redirection Test (DART [14]) by NASA aimed at demonstrating a method for planetary defense. In 2022, DART collided with Dimorphos, a satellite of the asteroid Didymos, and shortened its orbital period by 32 minutes, proving the effectiveness of the transfer of momentum from the S/C to the asteroid. The trajectories of these probes were designed using a variety of techniques, including patched-conics, gravity assist, impulsive and continuous-thrust maneuvers. The most relevant performance figures of these missions are summarized in Table 1.

Mission	Technique	Launch C_3 (km^2/s^2)	Δt (year)	ΔV (m/s)	Outcome	V_r (km/s)
NEAR [15]	GA/PC	25.9	5.0	1176	SL	0
Deep Impact [7]	HT	11.75	~ 0.5	-	FB+I	10
EPOXI [9]	GA/PC	extension	8.0	~ 150	FB+I	12.3
Hayabusa [8]	LT	-	2.5	-	SL	0.0
Chang'e 2 [10]	via Moon + L_2 Lissajous	2.2	677	-	FB	10.7
Hayabusa 2 [11]	GA/LT	21.0	3.6	~ 2000	SL	0.0
OSIRIS-Rex [12]	GA/HT	29.3	2.4	~ 900	SL	0.0
DART [16]	HT/LT	-	0.8	-	FB+I	6.0

Table 1: Trajectory information of past missions to NEOs: transfer technique, launch C_3 , time of flight to destination (Δt), ΔV budget of deterministic maneuvers, target approach mode (outcome) and velocity relative to target at arrival (V_r). Meaning of abbreviations and symbols: GA = gravity assist; PC = patched conics; HT = high thrust; LT = low thrust; FB = flyby; SL = soft landing; I = impact; - = data not found.

The Asteroid Redirect Mission (ARM [17]) was a solar-electric propulsion mission proposed by NASA to rendezvous with a large NEA (2011 MD was a prime candidate), use robotic arms to retrieve a 4-meter boulder, and bring it into lunar orbit. In fact, methods to rendezvous, retrieve and deliver portions or entire asteroids to near-Earth space are a major focus of investigations in the context of missions to NEOs. The trajectory design approaches include

conventional patched-conics, direct Lambert arcs and gravity assist (GA), and the propulsion can be chemical (high thrust, HT) or electrical (low-thrust, LT) (see, e.g., [18, 19, 20, 21, 22]). Notably, Strange et al. [23] provide an extensive list of NEAs reachable with HT or LT, directly or via GAs, between 2020 and 2024 and accessible for rendezvous or sample collection and return. Human exploration of NEAs has gained a lot of interest too. Since 2012, NASA has been updating the Near-Earth Object Human Space Flight Accessible Target Study (NHATS) database of targets on orbits very close to Earth’s and reachable by a round-trip mission of limited duration [24]. The trajectory design is carried out with the method of patched-conics, and employs full-precision ephemerides for both the S/C and the asteroids. Recently, Sánchez & Yáñez [25] proposed a method to drive objects from accessible heliocentric orbits into the Earth’s neighborhood using LT and the stable invariant manifolds of Lyapunov and halo orbits. Jorba & Nicolás [26] focused on the capture of NEAs by means of approximations of the stable manifolds of hyperbolic tori associated with the L_3 point of the Earth-Moon system in the planar Earth-Moon-Sun bicircular problem.

The use of low-energy trajectories to construct direct transfers and rendezvous opportunities with NEOs has not been addressed in a systematic way. This work offers a simple approach to identify and design this type of solution. The method exploits the dynamical and geometrical features of the hyperbolic invariant manifolds associated with periodic orbits around the collinear equilibrium points L_1 and L_2 of the Sun-Earth circular restricted three-body problem (CR3BP). These trajectories extend into near-Earth space both inside and outside of the terrestrial orbit. They also acquire a phase difference with respect to Earth’s motion, spanning a wide range of orbital domains and coming in close proximity to many resident objects. This is evidenced by Fig. 1, depicting the paths of unstable hyperbolic invariant manifolds associated with planar Lyapunov orbits (PLOs) around L_1 (red) and L_2 (blue) in the Sun-Earth rotating reference frame (left), and the orbits of several NEOs together with the terrestrial planets (right). These natural pathways are characterized by low en-

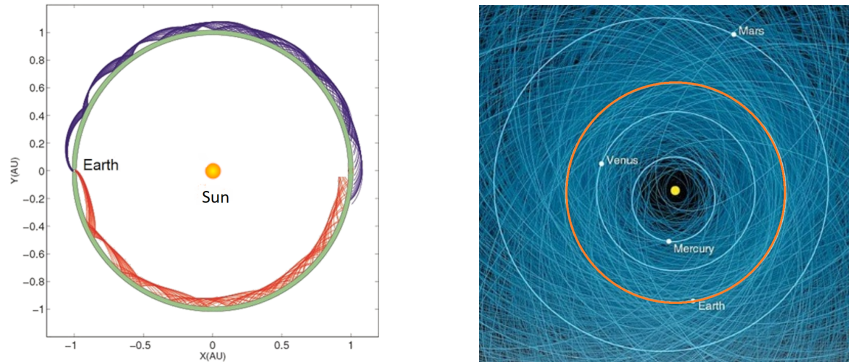


Figure 1: Left: propagation of branches of hyperbolic invariant manifolds associated with PLOs around L_1 (red) and L_2 (blue) in the Sun-Earth rotating reference frame (the green ring represents the forbidden region for the specific energy level considered). Right: orbits of several NEOs and the terrestrial planets.

ergies, i.e., low velocities with respect to Earth, which makes them accessible at very low launch cost. A key feature of the method is the approximation of these three-body trajectories with heliocentric two-body (2BP) ellipses beyond a certain distance from Earth. This technique, also called patched CR3BP/2BP model, was developed to design low-energy transfers between Galilean moons, simplifying the computation of connections between invariant manifold trajectories departing and approaching pairs of moons [27, 28, 29, 30]. In a similar way, in this work the encounter between the S/C and a NEO occurs at the intersection between the heliocentric osculating Keplerian orbits of the two bodies, and the rendezvous becomes a simple analytical problem. An impulsive maneuver at an intersection point yields a zero relative velocity encounter between the S/C and the target. Since the initial conditions of the trajectory of the S/C are generated in the Sun-Earth synodic barycentric reference frame, the orientation in space of the corresponding heliocentric ellipse varies linearly with the departure epoch. This feature provides a degree of freedom enabling the selection of the most desirable solutions, for example on the basis of the ΔV budget or the transfer time Δt . The methodology was developed in the planar approximation for low-inclination targets, and subsequently extended to 3D solutions.

The paper starts with the definition of the dynamical model for the S/C (Sect. 2). Section 3 deals with the selection of the target NEOs and the processing of their orbital data. Sections 4 and 5 present the methodology and results for planar and 3D transfers, respectively. Section 6 compares their performance against conventional patched-conics trajectories. Section 7 summarizes and concludes the paper. Preliminary explorations of the method can be found in Donnarumma [31], and have been presented at the 2nd International Stardust Conference [32] and at the 74th International Astronautical Congress [33].

2. Dynamical model

The motion of the S/C starts in the vicinity of the Earth and is governed by the gravitational attraction of the Sun (mass M_S) and the Earth (mass M_E), i.e., the dynamical model is the Sun-Earth-S/C CR3BP. If the gravitational constant G , the sum $M_S + M_E$ and the distance d between the primaries are used as reference magnitudes, the mean motion of the primaries becomes unitary and their orbital period equals 2π . In the synodic barycentric reference frame, the Sun and the Earth are located at $(\mu, 0, 0)$ and $(\mu - 1, 0, 0)$, where μ denotes the mass ratio $M_E/(M_S + M_E)$ of the system (see Fig. 2). Table 2 lists the relevant physical parameters of the Sun-Earth system.

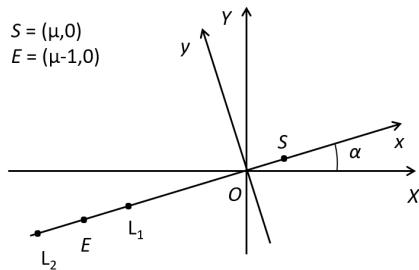


Figure 2: The Sun-Earth synodic barycentric reference frame (Oxy , rotating frame) and the barycentric ecliptic J2000.0 reference frame (OXY , inertial frame). O is the barycenter of the Sun-Earth system, S the Sun and E the Earth.

Symbol	Definition	Value	Units
GM_S	Sun's gravitational parameter	$1.3271244 \cdot 10^{11}$	km^3/s^2
GM_E	Earth's gravitational parameter	$3.9860044 \cdot 10^5$	km^3/s^2
R_E	Earth's equatorial radius	6378.1366	km
μ	Earth-Sun mass ratio	$0.30034806 \cdot 10^{-5}$	-
d	Earth-Sun distance	149597870	km

Table 2: Physical parameters of the Sun-Earth system used in this work [34].

Figure 3 illustrates families of PLOs around the two collinear equilibrium points L_1 and L_2 . Each set contains 50 orbits equally spaced in Jacobi constant C_J between 3.00056 (y amplitude $\simeq 3 \cdot 10^6$ km) and 3.00089 (y amplitude $\simeq 9 \cdot 10^3$ km).

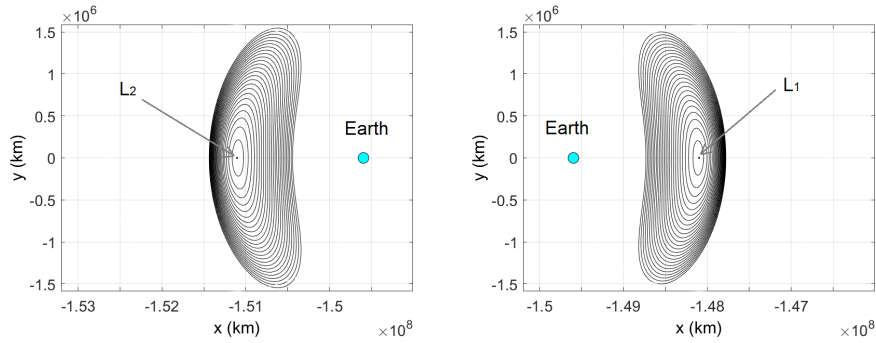


Figure 3: Families of 50 PLOs around L_2 (left) and L_1 (right) in the synodic barycentric reference frame.

The PLOs serve to generate two types of trajectories:

- Outward branches of hyperbolic invariant manifolds (MTs) (200 trajectories for each PLO). They are determined and propagated using standard methods. An initial state is generated by applying a small perturbation in the outward direction of the unstable eigenvector of the monodromy matrix of the PLO after appropriate time transformation through the state transition matrix (see e.g., [35]), followed by globalization of the manifold

by forward time propagation;

- Transit orbits (TOs), obtained from 70×70 equally-spaced points of a rectangular grid bounding the PLO (Fig. 4). Each point internal to the PLO (orange markers) is the start of a TO with the same C_J as the PLO. The direction of the initial velocity is parallel (L_1) or anti-parallel (L_2) to the x -axis¹. In this way, the TOs drive the S/C away from the Earth forward in time along paths contained in the outward invariant manifold branch with the same C_J . The initial states of the TOs are propagated backwards in time (i.e., towards the Earth). The trajectories that cross a circular parking orbit at 300 km altitude are retained (red markers in Fig. 4), the others are discarded. Figure 5 shows the characteristic launch energies (C_3) of the retained TOs, computed in the Earth-S/C 2BP. The number of retained TOs varies with the amplitude (hence, the value of C_J) of the PLO. Only the first 20 Lyapunov orbits of each family provide solutions that reach Earth’s vicinity (Fig. 6).

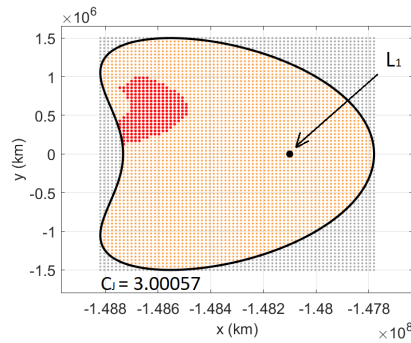


Figure 4: Generation of initial conditions for TOs inside a PLO with $C_J = 3.00057$: initial 70×70 grid (gray), internal points (orange), accepted internal points that connect with a 300-km altitude circular orbit around the Earth (red). For the sake of clarity, the two axes have been drawn with different scales.

¹Other choices are possible because the position and the Jacobi constant only constrain the magnitude of the velocity.

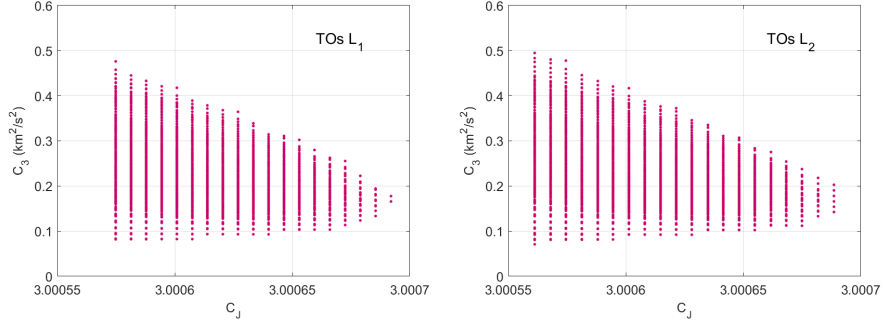


Figure 5: Characteristic launch energies of the TOs associated with L_1 (left) and L_2 (right).

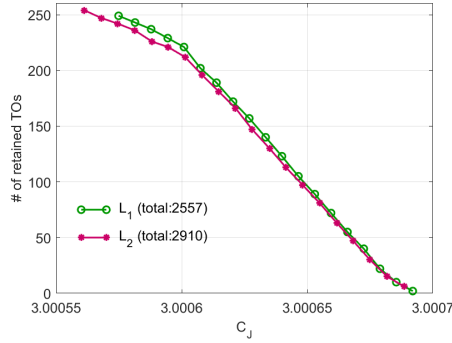


Figure 6: Number of TOs that reach a 300 km Earth's parking orbit per equilibrium point as a function of C_J .

The accepted TOs and all the MTs are propagated forward in time until they intersect an Earth-centered circle, called circle of influence (CI, Fig. 7) whose radius r_{CI} equals 2 773 940 km or three times $r_{SoI} = d (M_E/M_S)^{2/5}$, the radius of the Laplace sphere of influence of the Earth. This choice ensures that the CI encloses all the PLOs of the two families, as shown in Fig. 8.

MTs and TOs represent different mission opportunities. MTs can be used, for example, to depart the vicinity of an equilibrium point, whereas TOs are direct trajectories from a geocentric parking orbit. The two types span the same energy levels, but while MTs initially stay close to the LPO, TOs pass through it and reach the CI directly, resulting in faster transfers (see Fig. 9).

The state vectors of MTs and TOs at the CI are collected and transformed

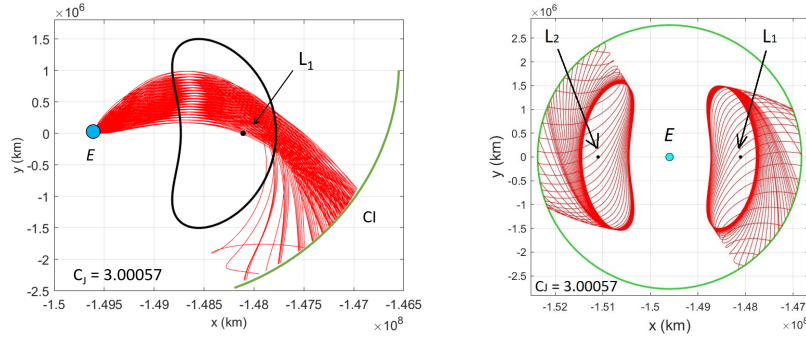


Figure 7: Left: propagation of TOs from the the accepted grid points towards the parking orbit (backward) and the CI (forward). Right: forward propagation of the outward branches of two MTs until they cross the CI.

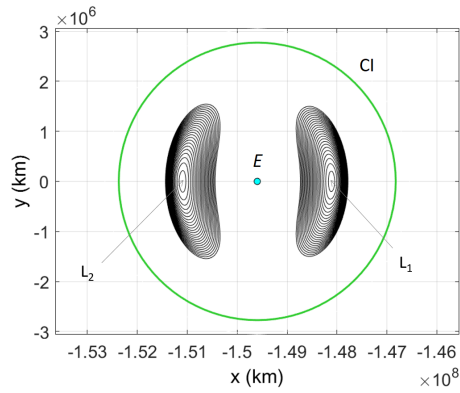


Figure 8: The two families of PLOs and the CI.

to the heliocentric ecliptic J2000.0 reference frame. In this operation, the distance between the barycenter of the Sun-Earth system and the center of the Sun is neglected. The longitude of the perihelion of the osculating heliocentric ellipses depends on the date of CI crossing, and varies at a constant rate equal to the mean motion n_{ES} of the Sun-Earth system. Semimajor axis, eccentricity and true anomaly depend entirely on the state vector at the CI in the synodic frame. This is sketched in Fig. 10 which shows two osculating ellipses corresponding to the same three-body state vector at two different CI crossing times, t_1 and t_2 (resulting from two different departure dates on the same CR3BP

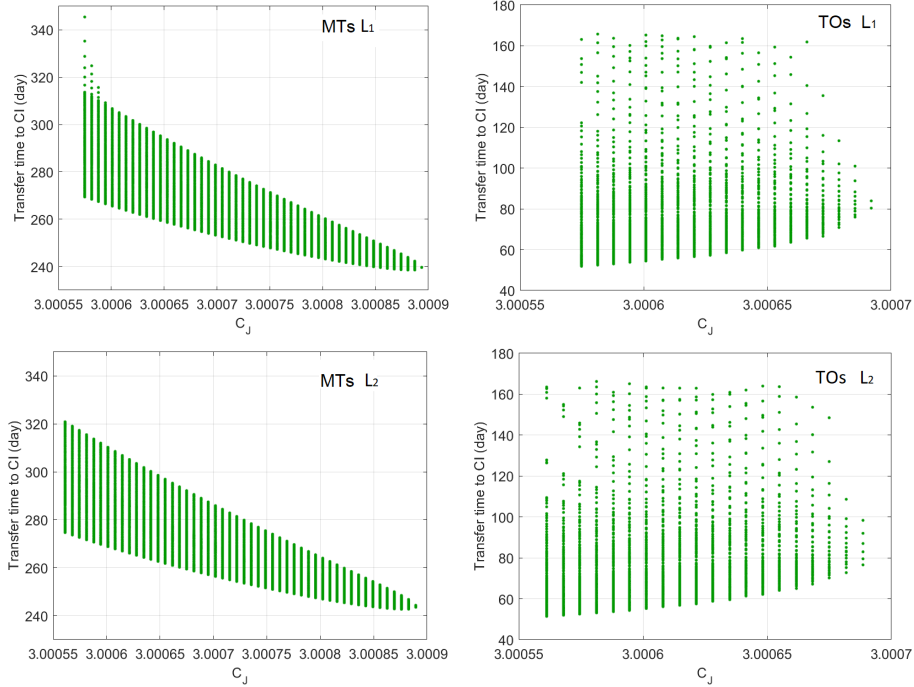


Figure 9: Transfer times from each departure location to the CI for each trajectory type.

trajectory). The shapes of the two orbits are identical, and they share the same true anomaly at CI crossing. The directions of the lines of apsides are related through $\omega_{S/C}(t_2) = \omega_{S/C}(t_1) + n_{ES}(t_2 - t_1)$, where $\omega_{S/C}$ is the longitude of the perihelion of the S/C's orbit. The value of this parameter depends on the angle (α in Fig. 2) between the synodic frame and the inertial frame at the time of CI crossing. This angle is zero at the Spring Equinox, whose reference epoch is 2460024.3917 JD = 2023-Mar-20 21:24:00 UTC. This date is used to determine the instantaneous orientation of the x -axis of the synodic frame.

3. NEOs: orbital data and dynamical model

The orbital parameters of the candidate targets for rendezvous have been extracted from the Solar System Dynamics Minor Bodies Database [36], which on July 30, 2023 listed orbital data for 32 396 asteroids and comets with perihelion

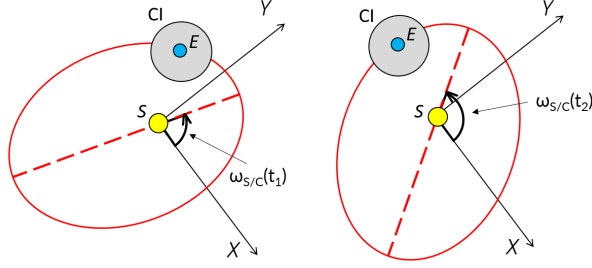


Figure 10: Effect of the CI crossing time ($t_1 < t_2$) on the longitude of the perihelion $\omega_{S/C}$ of an osculating heliocentric orbit obtained from the same CR3BP state vector at the CI.

below 1.3 au. Retaining only objects with ecliptic inclination $\leq 5^\circ$, perihelion distance ≥ 0.9 au and aphelion distance ≤ 1.1 au yields a set of 72 asteroids (Table 3). The semimajor axes range from 0.971 to 1.058 au, while the eccentricities span the interval $[0.039, 0.0898]$. Figure 11 shows the distribution of orbital inclinations and the intervals of heliocentric distances swept by the 72 orbits. All data are given in the heliocentric ecliptic J2000.0 reference frame with osculation epoch $t_0 = 2460000.5$ JD = 2023-Feb-25 00:00:00 UTC. The dynamical model for the NEOs is the Sun-asteroid 2BP.

1 = 459872	16 = 2012 LA	31 = 2017 FT102	46 = 2020 HO5	61 = 2022 NX1
2 = 1991 VG	17 = 2012 TF79	32 = 2017 HU49	47 = 2020 MU1	62 = 2022 OB5
3 = 2000 SG344	18 = 2013 BS45	33 = 2018 FM3	48 = 2020 RB4	63 = 2022 RS1
4 = 2003 YN107	19 = 2013 GH66	34 = 2018 PK21	49 = 2020 VN1	64 = 2022 RD2
5 = 2006 JY26	20 = 2013 RZ53	35 = 2018 PN22	50 = 2020 WY	65 = 2022 RW3
6 = 2006 QQ56	21 = 2014 DJ80	36 = 2018 PM28	51 = 2021 AT2	66 = 2023 FY3
7 = 2006 RH120	22 = 2014 QD364	37 = 2018 WV1	52 = 2021 AK5	67 = 2023 GQ1
8 = 2008 KT	23 = 2014 WU200	38 = 2019 FV2	53 = 2021 CZ4	68 = 2023 GT1
9 = 2008 UA202	24 = 2014 WX202	39 = 2019 GF1	54 = 2021 GM1	69 = 2023 HM4
10 = 2010 JW34	25 = 2015 JD3	40 = 2019 KJ2	55 = 2021 LF6	70 = 2023 HG11
11 = 2010 VQ98	26 = 2015 XZ378	41 = 2019 PO1	56 = 2021 RZ3	71 = 2023 LE
12 = 2011 BL45	27 = 2016 GK135	42 = 2020 CD3	57 = 2021 RG12	72 = 2023 LG2
13 = 2011 MD	28 = 2016 RD34	43 = 2020 FA1	58 = 2021 VH2	
14 = 2011 UD21	29 = 2016 YR	44 = 2020 GE	59 = 2021 VX22	
15 = 2012 FC71	30 = 2017 BN93	45 = 2020 HF4	60 = 2022 BY39	

Table 3: Candidate targets: primary designation and object index assigned in this work.

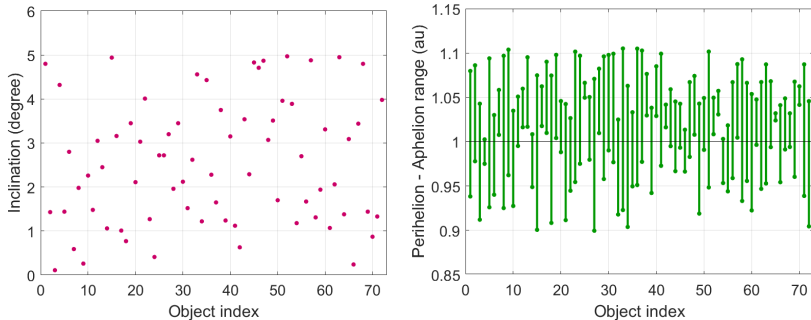


Figure 11: Orbital inclinations (left) and perihelion - aphelion ranges (right) of the 72 selected NEOs.

4. Planar impulsive rendezvous

Neglecting the gravitational attraction of the Earth outside the CI transforms the design of a direct transfer to a NEO into a search for intersections between confocal ellipses. In the planar approximation, the selected low-inclination targets and the S/C move in the ecliptic plane. Hence, the rendezvous occurs at the intersection between their coplanar confocal elliptical orbits. The solution of this mathematical problem is due to [37] and was recently applied to design transfers between giant planet moons [27, 28, 29, 30]. The semimajor axis and the eccentricity of the orbits of the two bodies, and the angle between the two periapses determine the number of intersection points. As shown in Fig. 12, which portrays two elliptical orbits with their arguments of perihelion ω_{NEO} and $\omega_{S/C}$, the number of intersection points can be 0, 1 (tangential intersections $A = B$) or 2 ($A \neq B$) depending on the relative sizes and orientations of the ellipses. The tangential case corresponds to the rendezvous impulse $\Delta \mathbf{V}_{\#} = \mathbf{V}_{S/C} - \mathbf{V}_{NEO}$ with the smallest magnitude (see, e.g., [27]).

The longitude of the orbit perihelion for the NEO is fixed at the value corresponding to the osculation epoch. For the S/C this quantity is a function of the CI crossing date, which ultimately depends on the departure date. The latter is computed *a posteriori* on the basis of the rendezvous requirements,

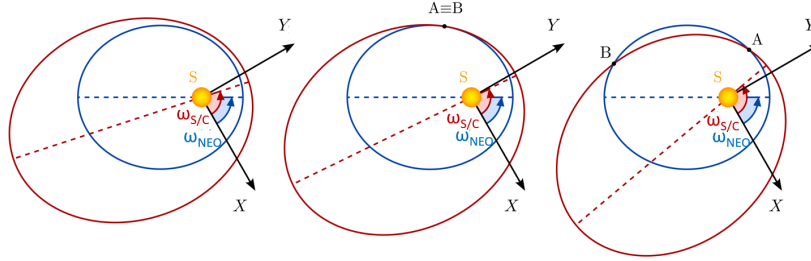


Figure 12: Number of intersection points between confocal coplanar ellipses for different mutual orientations: 0 (left), 1 (center), 2 (right).

as shown later². The range of values of the longitude of the perihelion of the orbit of the S/C for which intersections with the target orbit exist can be determined analytically (see [27]). This range is sampled with a uniform step $\Delta\omega$, and each value (denoted ω_d meaning desired ω) is used to compute the position of the intersection point(s) between the elliptical orbits. The time of passage of the target NEO through the rendezvous point determines the rendezvous date $t_{\#}$ (Fig. 13 left). From this epoch, the (desired) time t_{CI} of CI crossing is computed. This date is associated with a value (denoted ω_r or real ω) of the longitude of the perihelion of the S/C orbit. A non-zero $\omega_e = |\omega_d - \omega_r|$ yields a non-zero rendezvous distance $\Delta r_{\#}$ between the S/C and the target at $t_{\#}$ (Fig. 13 middle). $\Delta r_{\#}$ depends on ω_e and the eccentricity of the two orbits. In the limit case of zero eccentricity and orbital radius = r for both the S/C and the target, $\Delta r_{\#} = 2r \sin(\omega_e/2)$, which for $\omega_e = 0.01^\circ$ and $r = 1$ au gives $\Delta r_{\#} \simeq 10^4$ km. Therefore, limiting the value of ω_e (by discarding solutions for which this quantity exceeds a pre-assigned threshold) leads to encounters with an acceptable close-approach distance $\Delta r_{\#}$. Then, $\Delta V_{\#}$ and the total transfer time Δt can be used to characterize the performance of a rendezvous trajectory with the given target.

Note that $\Delta r_{\#}$ can be reduced to zero, for instance, by computing the Lam-

²The autonomous character of the CR3BP ensures freedom in the choice of the departure date.

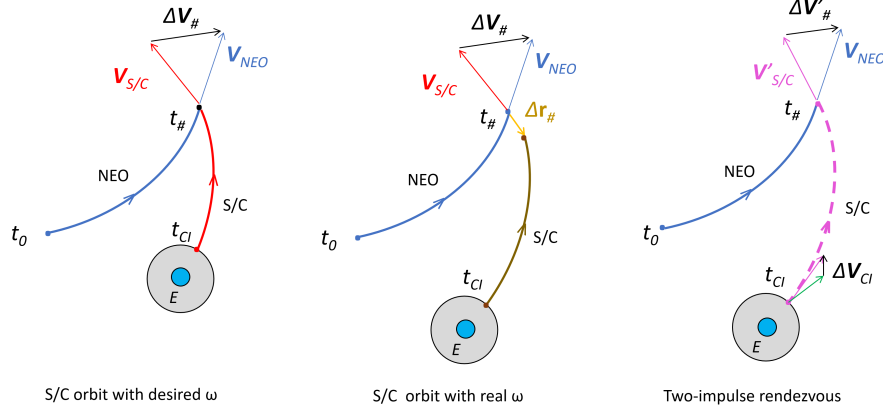


Figure 13: Left: Ideal S/C transfer and rendezvous with $\omega_{S/C} = \omega_d$. Middle: real S/C transfer with $\omega_{S/C} = \omega_r$. Right: Two-impulse transfer through the solution of Lambert’s problem between t_{CI} and $t_{\#}$.

bert arc between the position of the S/C at t_{CI} and that of the asteroid at $t_{\#}$, leading to a two-impulse transfer, i.e., $\Delta\mathbf{V}_{CI}$ at the CI and $\Delta\mathbf{V}'_{\#}$ at rendezvous (Fig. 13 right). Alternatively, $\Delta r_{\#}$ can be reduced or eliminated by replacing the impulsive rendezvous maneuver ($\Delta\mathbf{V}_{\#}$) with a LT transfer.

The strategy outlined above has been applied to all the combinations of target orbits and S/C trajectories (MTs and TOs from L_1 and L_2). The simulations have been conducted with sampling intervals $\Delta\omega$ of 0.4° and $\omega_e = 0.02^\circ$. Setting an upper limit of 1500 m/s on the magnitude of $\Delta\mathbf{V}_{\#}$ yields close to 70 000 rendezvous trajectories to a subset of 24 asteroids from the initial list. Table 4 lists the number of solutions and the features of the transfers with the best performance for each target and trajectory type: i.e., minimum $\Delta V_{\#}$ ($\Delta V_{\#m}$) and corresponding transfer time, minimum Δt (Δt_m) and corresponding rendezvous impulse, and the minimum $\Delta r_{\#}$ ($\Delta r_{\#m}$). Figure 14 illustrates six solutions from the set. Table 5 compares the magnitude $\Delta V_{\#}$ of the rendezvous maneuver with the cost of the two-impulse transfer (ΔV_{CI} , $\Delta V'_{\#}$) for the six cases portrayed in Fig. 14.

Ind.	No. of solutions MT-L1/MT-L2 /TO-L1/TO-L2	MT-L1			MT-L2			TO-L1			TO-L2		
		$\Delta V_{\#m}(\Delta t)$ m/s (day)	$\Delta t_m/(\Delta V)$ day (m/s)	$\Delta r_{\#m}$ km	$\Delta V_{\#m}(\Delta t)$ m/s (day)	$\Delta t_m/(\Delta V)$ day (m/s)	$\Delta r_{\#m}$ km	$\Delta V_{\#m}(\Delta t)$ m/s (day)	$\Delta t_m/(\Delta V)$ day (m/s)	$\Delta r_{\#m}$ km	$\Delta V_{\#m}(\Delta t)$ m/s (day)	$\Delta t_m/(\Delta V)$ day (m/s)	$\Delta r_{\#m}$ km
35	609/0/34/0	357 (392)	354 (491)	82	-	-	-	419 (300)	250 (543)	1973	-	-	-
39	684/0/0/0	716 (554)	478 (990)	17	-	-	-	-	-	-	-	-	-
44	0/882/0/198	-	-	-	344 (402)	340 (535)	9	-	-	-	359 (254)	186 (549)	5
45	0/2981/0/0	-	-	-	378 (666)	552 (994)	92	-	-	-	-	-	-
46	8042/0/5157/0	405 (643)	470 (818)	8	-	-	-	405 (419)	310 (997)	1	-	-	-
47	0/330/0/0	-	-	-	676 (675)	637 (922)	113	-	-	-	-	-	-
49	1488/0/7/0	464 (468)	399 (921)	10	-	-	-	572 (334)	324 (811)	8905	-	-	-
50	0/2060/0/0	-	-	-	558 (717)	540 (991)	134	-	-	-	-	-	-
52	0/1737/0/0	-	-	-	394 (693)	604 (995)	3	-	-	-	-	-	-
54	2065/0/34/0	332 (612)	531 (997)	12	-	-	-	500 (480)	463 (702)	11848	-	-	-
55	1214/0/0/0	596 (564)	476 (996)	16	-	-	-	-	-	-	-	-	-
56	0/1025/0/10	-	-	-	585 (550)	484 (994)	1	-	-	-	593 (448)	395 (996)	2344
59	0/1251/0/43	-	-	-	492 (543)	447 (859)	161	-	-	-	499 (395)	356 (750)	128
61	0/3058/0/209	-	-	-	133 (530)	427 (357)	34	-	-	-	130 (378)	301 (271)	96
63	0/375/0/0	-	-	-	624 (582)	498 (996)	301	-	-	-	-	-	-
64	0/1076/0/24	-	-	-	133 (513)	416 (240)	18	-	-	-	132 (359)	339 (174)	1329
65	0/116/0/49	-	-	-	152 (513)	510 (164)	305	-	-	-	168 (354)	330 (173)	4724
66	0/6233/0/814	-	-	-	432 (397)	277 (995)	2	-	-	-	447 (152)	98 (644)	5
67	0/8065/0/206	-	-	-	381 (402)	299 (814)	26	-	-	-	599 (268)	216 (939)	280
68	0/6183/0/5307	-	-	-	133 (407)	265 (585)	7	-	-	-	131 (160)	90 (566)	10
69	0/4767/0/65	-	-	-	462 (376)	295 (930)	1	-	-	-	694 (281)	236 (711)	129
70	0/2562/0/84	-	-	-	244 (381)	320 (542)	3	-	-	-	275 (280)	229 (500)	731
71	0/1560/0/49	-	-	-	548 (411)	323 (911)	59	-	-	-	590 (274)	231 (959)	19
72	15/0/0/0	979 (409)	398 (997)	455	-	-	-	-	-	-	-	-	-

Table 4: Characteristics of the best planar rendezvous trajectories to the selected NEAs. The solutions highlighted in boldface are illustrated in Fig. 14.

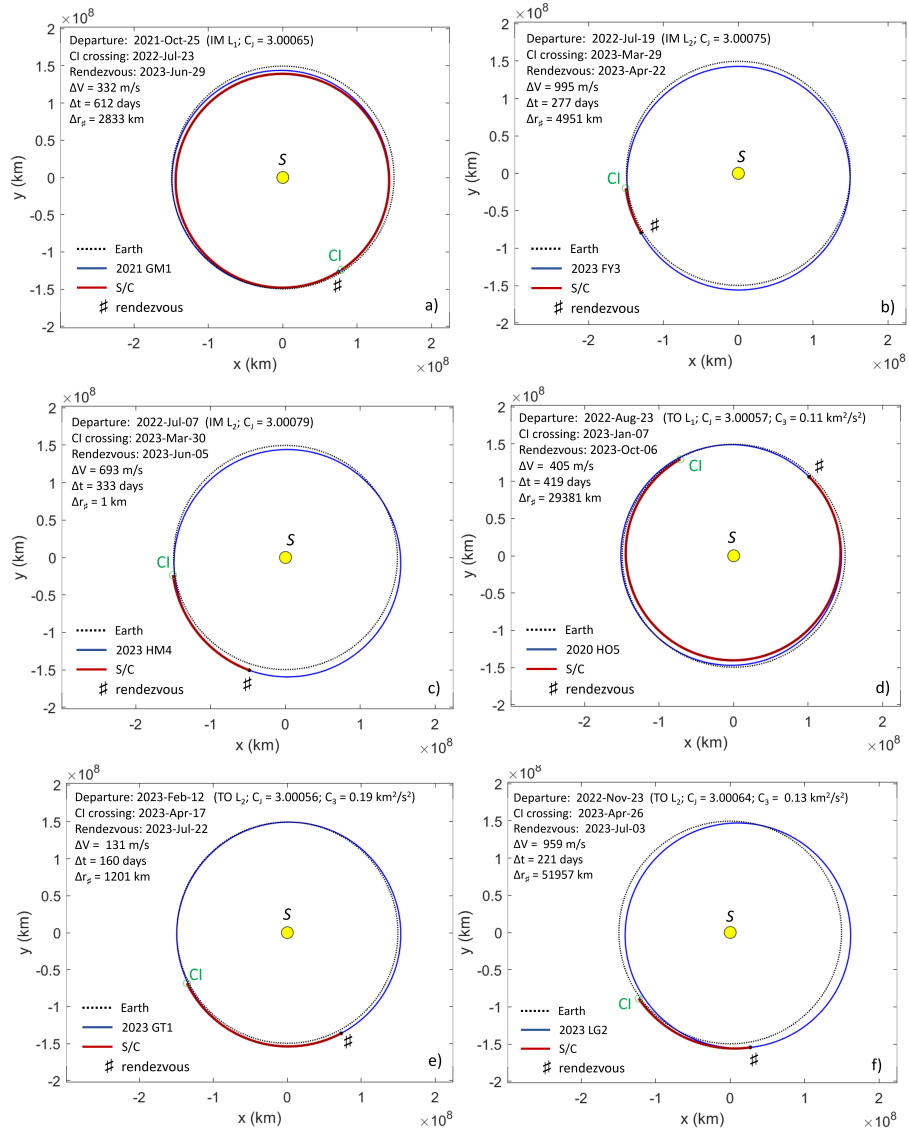


Figure 14: Examples of planar rendezvous trajectories.

5. Extension to 3D impulsive rendezvous trajectories

Impulsive rendezvous trajectories taking into account the 3D orientation (inclination, longitude of the ascending node, argument of perihelion) of the

Case	$\Delta V_{\#}$ (m/s)	ΔV_{CI} (m/s)	$\Delta V'_{\#}$ (m/s)
a	332.1	0.46	332.6
b	995.5	20.5	992.8
c	693.6	1.11	694.6
d	405.7	0.15	405.5
e	131.9	0.03	131.9
f	959.5	10.1	962.2

Table 5: Magnitude of the rendezvous maneuver (second column) and cost of the two-impulse transfer (third and fourth column) for the six cases portrayed in Fig. 14.

orbit of the candidate NEO have been designed by computing the intersections between confocal non-coplanar elliptical orbits, one with fixed orbital elements (NEO) and the other lying on the ecliptic plane and oriented as determined by the date of CI crossing. Under this assumption, the intersection must occur at either node of the target’s orbit. However, the correct phasing is not guaranteed *a priori*. The algorithm adjusts the CI crossing date (which determines the departure date) and calculates a ballistic heliocentric arc connecting the CI with a node of the target’s orbit. A Lambert solver computes the necessary impulses at the CI ($\Delta \mathbf{V}_1$) and the rendezvous point ($\Delta \mathbf{V}_2$) (see Fig. 15).

The simulations consider both types of trajectories (MTs and TOs) using a discretization of 5 days for the CI crossing date and setting bounds of 2.5 km/s for the total transfer impulse ($\Delta V = \Delta V_1 + \Delta V_2$) and 1.2 years for the time of flight. The results are summarized in Tables 6 and 7, which for each accessible target and trajectory type yields the number of solutions obtained, minimum ΔV (ΔV_m) and corresponding transfer time, fastest transfer (Δt_m) and corresponding ΔV . Figure 16 illustrates the ecliptic projection and the 3D view of two trajectories.

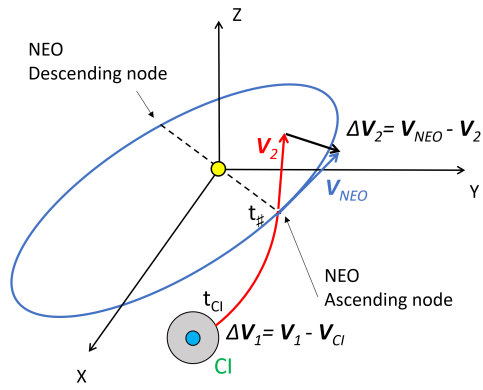


Figure 15: Schematic representation of a two-impulse transfer to rendezvous with a target in an inclined orbit. The encounter takes place at one of the nodes.

Index	No. of solutions MT-L ₁ /MT-L ₂ /TO-L ₁ /TO-L ₂	MT-L ₁		MT-L ₂		TO-L ₁		TO-L ₂	
		$\Delta V_m / (\Delta t)$ m/s (day)	$\Delta t_{m_i} / (\Delta V)$ day (m/s)	$\Delta V_m / (\Delta t)$ m/s (day)	$\Delta t_{m_i} / (\Delta V)$ day (m/s)	$\Delta V_m / (\Delta t)$ m/s (day)	$\Delta t_{m_i} / (\Delta V)$ day (m/s)	$\Delta V_m / (\Delta t)$ m/s (day)	$\Delta t_{m_i} / (\Delta V)$ day (m/s)
2	2878/ 5254/ 0/ 0	1189 (88)	11 (1558)	769 (136)	65 (1924)	-	-	-	-
3	2349/ 2829/ 0/ 0	941 (249)	97 (2463)	1284 (273)	46 (2443)	-	-	-	-
4	0/ 0/ 84/ 0	-	-	-	-	2321 (346)	49 (2443)	-	-
5	1349/ 2172/ 0/ 0	2161 (344)	158 (2495)	2188 (337)	57 (2498)	-	-	-	-
6	0/ 0/ 61/ 54	-	-	-	-	1575 (193)	116 (2069)	1679 (296)	43 (2208)
7	0/ 0/ 983/ 1077	-	-	-	-	853 (204)	182 (971)	574 (184)	45 (782)
8	692/ 1810/ 0/ 0	2263 (326)	180 (2482)	2078 (313)	181 (2463)	-	-	-	-
9	0/ 0/ 275/ 616	-	-	-	-	1331 (275)	11 (2009)	965 (294)	207 (2175)
10	0/ 1/ 46/ 47	-	-	2320 (98)	98 (2320)	1483 (114)	83 (2012)	2153 (136)	136 (2153)
11	1159/ 3/ 0/ 0	1904 (315)	10 (2365)	1692 (39)	33 (2347)	-	-	-	-
12	0/ 0/ 32/ 127	-	-	-	-	2237 (209)	124 (2375)	1545 (219)	131 (2378)
13	0/ 0/ 0/ 189	-	-	-	-	-	-	1817 (55)	55 (1817)
14	0/ 0/ 100/ 144	-	-	-	-	640 (122)	89 (753)	1168 (333)	186 (1562)
16	0/ 0/ 8/ 79	-	-	-	-	2351 (221)	175 (2470)	1658 (289)	58 (2388)
17	0/ 0/ 427/ 506	-	-	-	-	1313 (134)	130 (1330)	737 (288)	93 (2190)
18	0/ 0/ 752/ 840	-	-	-	-	1503 (260)	239 (1673)	1323 (245)	96 (2493)
19	0/ 0/ 151/ 243	-	-	-	-	2275 (245)	220 (2348)	1949 (360)	125 (2357)
20	1952/ 2880/ 0/ 0	1433 (280)	162 (1591)	1157 (71)	22 (1446)	-	-	-	-
21	0/ 0/ 46/ 21	-	-	-	-	2028 (150)	119 (2438)	2014 (151)	150 (2285)
22	0/ 0/ 135/ 415	-	-	-	-	2429 (172)	166 (2434)	2150 (27)	19 (2321)
23	2835/ 1947/ 0/ 0	1496 (31)	15 (2180)	897 (97)	62 (2392)	-	-	-	-
24	2137/ 0/ 0/ 0	1567 (331)	82 (2289)	-	-	-	-	-	-
25	0/ 0/ 41/ 89	-	-	-	-	2200 (181)	167 (2283)	1460 (208)	100 (2305)
26	519/ 971/ 0/ 0	1798 (122)	102 (1821)	1720 (253)	67 (2353)	-	-	-	-
28	0/ 724/ 5/ 0	-	-	1215 (56)	44 (2120)	2327 (280)	275 (2474)	-	-
29	0/ 78/ 0/ 0	-	-	1978 (41)	34 (2434)	-	-	-	-
30	0/ 0/ 2/ 0	-	-	-	-	2424 (310)	305 (2439)	-	-

Table 6: Characteristics of the best 3D rendezvous trajectories to the selected NEAs with $\Delta V \leq 2500$ m/s and $\Delta t \leq 1.2$ years.

Index	No. of solutions MT-L ₁ /MT-L ₂ /TO-L ₁ /TO-L ₂	MT-L ₁		MT-L ₂		TO-L ₁		TO-L ₂	
		$\Delta V_m / (\Delta t)$ m/s (day)	$\Delta t_{m_i} / (\Delta V)$ day (m/s)	$\Delta V_m / (\Delta t)$ m/s (day)	$\Delta t_{m_i} / (\Delta V)$ day (m/s)	$\Delta V_m / (\Delta t)$ m/s (day)	$\Delta t_{m_i} / (\Delta V)$ day (m/s)	$\Delta V_m / (\Delta t)$ m/s (day)	$\Delta t_{m_i} / (\Delta V)$ day (m/s)
31	3788/ 3578/ 0/ 0	1610 (338)	158 (1881)	929 (91)	59 (2342)	-	-	-	-
32	0/ 0/ 220/ 164	-	-	-	-	1833 (180)	148 (2116)	1633 (286)	176 (2489)
34	0/ 0/ 0/ 2	-	-	-	-	-	-	2471 (217)	217 (2474)
36	779/ 473/ 0/ 0	1805 (192)	190 (2041)	1211 (158)	94 (2488)	-	-	-	-
37	2911/ 5761/ 0/ 0	1575 (210)	203 (2250)	856 (225)	139 (1754)	-	-	-	-
38	0/ 3325/ 0/ 0	-	-	1898 (123)	63 (2490)	-	-	-	-
39	0/ 0/ 27/ 157	-	-	-	-	2392 (332)	332 (2392)	2188 (358)	358 (2216)
40	533/ 3670/ 0/ 0	2329 (166)	148 (2467)	1608 (109)	71 (2366)	-	-	-	-
41	1574/ 2204/ 0/ 0	1427 (123)	123 (1427)	802 (59)	43 (2051)	-	-	-	-
42	591/ 889/ 0/ 0	833 (232)	165 (876)	796 (202)	58 (1636)	-	-	-	-
43	3/ 353/ 0/ 0	2315 (182)	182 (2315)	1924 (260)	152 (2428)	-	-	-	-
44	0/ 0/ 1/ 3	-	-	-	-	2419 (29)	29 (2419)	2126 (41)	29 (2133)
48	45/ 769/ 0/ 0	2146 (170)	162 (2387)	1566 (267)	23 (2196)	-	-	-	-
50	200/ 234/ 0/ 0	1180 (129)	129 (1180)	1419 (293)	267 (1925)	-	-	-	-
53	1/ 107/ 0/ 0	2485 (225)	225 (2485)	2100 (160)	58 (2459)	-	-	-	-
54	0/ 0/ 1/ 416	-	-	-	-	2472 (343)	343 (2472)	1568 (326)	323 (1616)
55	0/ 0/ 0/ 1	-	-	-	-	-	-	2324 (23)	23 (2324)
56	2/ 22/ 5/ 0	1892 (338)	336 (2337)	1945 (164)	140 (2477)	1566 (70)	36 (2018)	-	-
59	0/ 3/ 0/ 0	-	-	2449 (218)	218 (2456)	-	-	-	-
61	11/ 0/ 0/ 0	1762 (303)	290 (2439)	-	-	-	-	-	-
62	0/ 0/ 1/ 1	-	-	-	-	2435 (34)	34 (2435)	2219 (32)	32 (2219)
64	0/ 0/ 0/ 1	-	-	-	-	-	-	1983 (23)	23 (1983)
65	0/ 0/ 0/ 2	-	-	-	-	-	-	2078 (27)	27 (2078)
66	1/ 63/ 1/ 2	2481 (307)	307 (2481)	1840 (348)	334 (2495)	2143 (33)	33 (2143)	1356 (53)	29 (1543)
67	0/ 0/ 0/ 1	-	-	-	-	-	-	2297 (24)	24 (2297)
69	1/ 0/ 0/ 0	2352 (280)	280 (2352)	-	-	-	-	-	-
70	0/ 0/ 0/ 1	-	-	-	-	-	-	2050 (21)	21 (2050)
71	0/ 0/ 0/ 2	-	-	-	-	-	-	2335 (60)	60 (2335)

Table 7: Characteristics of the best 3D rendezvous trajectories to the selected NEAs with $\Delta V \leq 2500$ m/s and $\Delta t \leq 1.2$ years.

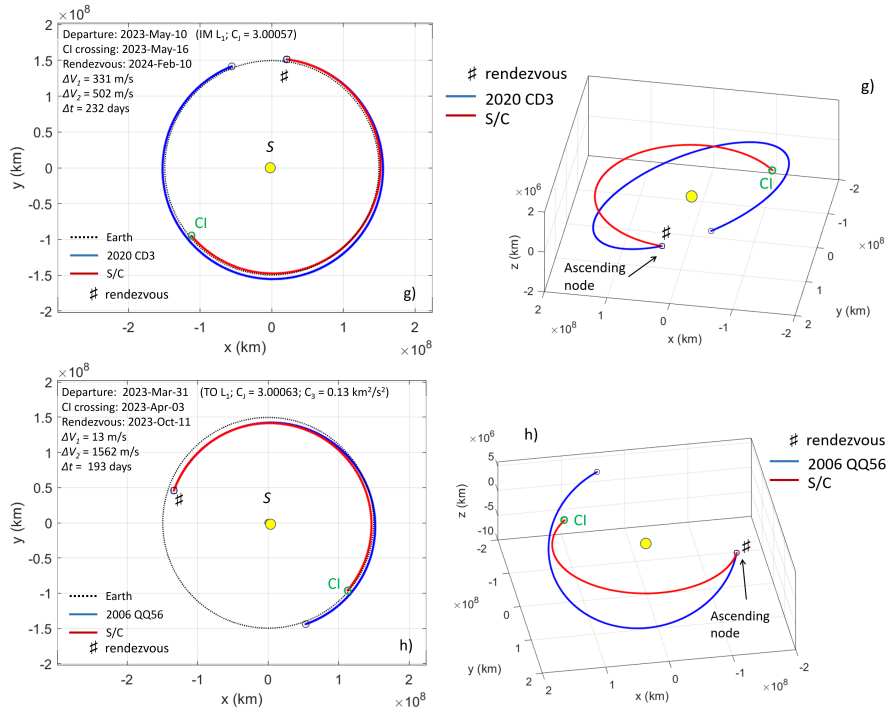


Figure 16: Example of spatial rendezvous trajectories: ecliptic projection (left) and 3D view (right).

6. Comparison with patched-conics solutions

The performance of the 3D low-energy impulsive transfers via TOs described in this contribution have been compared with the trajectories of the mission concept study carried out within NASA's Planetary Science Decadal Survey devoted to NEAs [23]. It provides direct, HT rendezvous trajectories with launch dates between 1-Jan-2020 and 1-Jan-2025, maximum flight time to the target of 5 years, launch C_3 below $25 \text{ km}^2/\text{s}^2$, and rendezvous ΔV under 3 km/s . NASA's solutions are computed using a simplified, suboptimal, patched-conics approximation and then optimized with respect to the delivered S/C mass at rendezvous via Sequential Quadratic Programming. The work of Strange et al. [23] was published in 2010, when the majority of the asteroids considered in this

work were yet to be discovered. As a result, the intersection of the two datasets contains only two targets: 2003 YN107 (object index 4) and 2006 QQ56 (object index 6). Table 8 compares total transfer ΔV , time of flight Δt and launch C_3 from Appendix C of [23] against the 3D TO/ L_1 transfers with the lowest ΔV (see Table 6) to the same targets. Note that the solutions by Strange et al. [23] launch approximately 2.5 years earlier than those obtained in this work.

The cost of the rendezvous with 2003 YN107 is significantly higher when traveling via a TO (2321 m/s versus 1250 m/s), but this disadvantage is partially offset by a lower launch energy. Assuming a 300-km altitude circular departure orbit, the two values of the launch energy ($0.13 \text{ km}^2/\text{s}^2$ and $6.30 \text{ km}^2/\text{s}^2$) map into departure ΔV 's of 3212 m/s and 3490 m/s. Thus, the net advantage of NASA's solution is 793 m/s. Note, however, that this comes at the expense of a much longer transfer duration (almost double). It is generally possible to reduce propellant consumption by increasing the time of flight, so it is not surprising that the longer transfer is more efficient. Note also that the search for feasible trajectories limited the time of flight to 1.2 years. The limit made it impossible to find a close match of NASA's solution, but it is not an intrinsic limitation of the methodology. Raising the maximum time of flight for the search enables revisiting the intersection points of the heliocentric ellipses once per orbital period of the S/C. Thus, additional phasing conditions can be analyzed for improved fuel-efficiency. This enables a comprehensive exploration of the solution space, making the technique quite versatile.

The trajectory to 2006 QQ56 proposed in this work (see also case h, Fig. 16) outperforms the solution by [23] in all aspects (shorter duration and lower total impulse). This demonstrates the ability of the new technique to find highly-efficient solutions, even when the time of flight is constrained. It is a valuable tool to expand the solution space covered by more traditional methods.

Object	2003 YN107 (index 4)		2006 QQ56 (index 6)	
	Ref. [23]	This work	Ref. [23]	This work
ΔV (m/s)	1250	2321	1885	1575
Δt (day)	621	346	621	193
C_3 (km ² /s ²)	6.30	0.13	5.90	0.13
Launch date	2019-Dec-19	2022-Mar-26	2020-Sep-02	2023-Mar-31
Arrival date	2021-Aug-26	2023-Mar-06	2022-May-07	2023-Oct-11

Table 8: Performance features of the direct rendezvous trajectories to the same two targets computed by Strange et al. [23] and in this work.

7. Discussion and conclusions

The present contribution proposes a simple and efficient technique to systematically generate low-energy impulsive rendezvous trajectories to Near-Earth Objects on low-eccentricity, low-inclination orbits. The dynamical model is the patched Sun-Earth circular restricted three-body problem / Sun-spacecraft two-body problem. Hence, the influence of the Sun is incorporated along the entire path. Two types of initial conditions are considered: departures from planar Lyapunov orbits around Sun-Earth L_1 or L_2 via outward branches of the associated hyperbolic invariant manifolds, and launches from a 300-km altitude circular orbit via selected transit orbits (trajectories internal to the same hyperbolic invariant manifolds). Thus, two mission scenarios are accommodated: direct Earth departures and transfers from an intermediate gateway near a Lagrange point. The two types of trajectories exhibit different performance characteristics, particularly in terms of time of flight. Earth departures are generally faster due to their specific geometrical characteristics.

The heliocentric osculating two-body orbit obtained by transforming the state of the spacecraft at the crossing of Earth’s sphere of influence lies on the ecliptic plane. The mean motion of the orbit of the Earth around the Sun along with the departure date determine the longitude of the perihelion of such orbit,

providing a fundamental degree of freedom (the optimization variable) of the method, which calculates geometrical intersections between the elliptical orbits of the spacecraft and the target (in the planar case, the latter is projected on the ecliptic). Thus, when the rendezvous conditions are met, the transfer requires a single impulsive maneuver at arrival, the cost of which depends on the choice of the intersection point used for the encounter. The extension of the method to inclined target orbits introduces a Lambert arc between the sphere of influence of the Earth and one of the nodes of the orbit of the target, requiring two impulses.

In 2D, the identification of the rendezvous conditions is an analytical problem that can be solved in closed form. The ΔV -optimal transfer automatically emerges from the variation of the departure date as part of the search for the rendezvous conditions. The simple dependence of the orbital elements of the heliocentric orbit of the spacecraft on the departure state and date helps reduce the computational burden. Furthermore, the propagation of transit orbits and invariant manifold trajectories to the boundary of the sphere of influence of the Earth needs to be carried out only once. All these features make the method computationally efficient. The entire simulation for 72 candidate targets using the full set of invariant manifolds and transit orbits through both libration points took approximately 40 minutes in a mid-range laptop when programmed in the Fortran language.

It is important to note that the method here described identifies all the direct rendezvous opportunities that exist in the selected conditions (resolution, tolerances and maximum allowed ΔV budget and transfer time) at the chosen energy levels and in the approximation offered by the dynamical model. Hence, an extension to include other types of departure conditions would lead to a general tool capable of generating optimal direct interplanetary trajectories.

The patched three-body/two-body approximation adopted is at least as accurate as the conventional patched-conics approach. Hence, it is suitable for feasibility analyses, and its results can be refined with an ephemeris model for higher-fidelity mission design. The impulsive maneuvers can be replaced with

low-thrust arcs without altering the transfer times (see [33]), reducing the propellant consumption due to the higher specific impulse. The direct rendezvous trajectories described in this contribution can be viewed also as the building blocks of more complex mission scenarios, such as sample return operations and asteroid tours. Furthermore, the ΔV budgets and transfer times easily meet with the requirements set by NASA on the search for targets accessible by crewed missions [24].

The 3D trajectories from Earth to two neighboring asteroids via transit orbits have been benchmarked against direct optimal patched-conics transfers from a NASA study of accessible targets [23]. The test demonstrated the potential of the new method to find solutions that compare favorably in terms of time or flight and/or propellant consumption relative to traditional approaches, while requiring only modest computational resources.

Acknowledgments

EF, RF and GD acknowledge Khalifa University of Science and Technology's internal grant CIRA-2021-65/8474000413. EF and RF have been partially supported by Technology Innovation Institute through grant ELLIPSE/8434000533. EF acknowledges projects PID2020-112576GB-C21 and PID2021-123968NB-I00 of the Spanish Ministry of Science and Innovation.

References

- [1] NASA Jet Propulsion Laboratory, Center for Near-Earth Objects Study - NEO Basics, <https://cneos.jpl.nasa.gov/about/basics.html>, (last accessed 25 Aug. 2023).
- [2] L. A. McFadden and R. P. Binzel, Near-Earth Objects, in: Lucy-Ann McFadden, P. R. Weissman and T. V. Johnson (Ed.), *Encyclopedia of the Solar System*, 2nd Edition, Elsevier, 2007, pp. 283–300.

- [3] N. Anthony, M. R. Emami, Asteroid engineering: The state-of-the-art of Near-Earth Asteroids science and technology, *Progress in Aerospace Sciences* 100 (2018) 1–17. doi:<https://doi.org/10.1016/j.paerosci.2018.05.001>.
- [4] J. M. Hedo, E. Fantino, M. Ruíz, J. Peláez, Minimum orbital intersection distance: an asymptotic approach, *Astronomy & Astrophysics* 633 (2020) A22. doi:<https://doi.org/10.1051/0004-6361/201936502>.
- [5] J. S. Lewis, *Mining the sky: untold riches from the asteroids, comets, and planets*, Addison-Wesley Publishing Company, Reading (MA), 1997.
- [6] L. Prockter, S. Murchie, A. Cheng, et al., The NEAR Shoemaker mission to asteroid 433 Eros, *Acta Astronautica* 51 (1) (2002) 491–500. doi:[https://doi.org/10.1016/S0094-5765\(02\)00098-X](https://doi.org/10.1016/S0094-5765(02)00098-X).
- [7] W. H. Blume, Deep Impact Mission Design, *Space Science Reviews* 117 (2005) 23–42. doi:<https://doi.org/10.1007/s11214-005-3386-4>.
- [8] M. Yoshikawa, J. Kawaguchi, A. Fujiwara, A. Tsuchiyama, The Hayabusa mission, in: A. Longobardo (Ed.), *Sample Return Missions*, Elsevier, 2021, pp. 123–146. doi:<https://doi.org/10.1016/B978-0-12-818330-4.00006-9>.
- [9] M.-K. J. Chung, B. Shyamkumar, S. R. Chesley, et al., EPOXI Trajectory and Maneuver Analyses, in: *AAS/AIAA Astrodynamics Specialist Conference*, Girdwood (AK), 2011, paper AAS 11-482.
- [10] L. Liu, Y. Lie, J.-F. Cao, et al., Mission design of the CHANG'E-2 asteroid exploration mission, *Journal of Astronautics* 35 (2014) 262–268. doi:<https://doi.org/10.3873/j.issn.1000-1328.2014.03.003>.
- [11] Y. Tsuda, T. Saiki, F. Terui, et al., Hayabusa 2 mission status: landing, roving, and cratering on asteroid Ryugu, *Acta Astronautica* 171 (2020) 42–54. doi:<https://doi.org/10.1016/j.actaastro.2020.02.035>.

- [12] D. S. Lauretta, S. S. Balram-Knutson, E. Beshore, et al., OSIRIS-REx: Sample Return from Asteroid (101955) Bennu, *Space Science Reviews* 212 (2017) 925–984. doi:<https://doi.org/10.1007/s11214-017-0405-1>.
- [13] B. Williams, P. Antreasian, E. Carranza, et al., OSIRIS-REx Flight Dynamics and Navigation Design, *Space Science Reviews* 214 (69) (2018). doi:<https://doi.org/10.1007/s11214-018-0501-x>.
- [14] A. S. Rivkin, A. F. Cheng, Planetary defense with the Double Asteroid Redirection Test (DART) mission and prospects, *Nature Communications* 14 (2023) 1003. doi:<https://doi.org/10.1038/s41467-022-35561-2>.
- [15] D. Dunham, J. McAdams, R. Farquhar, Near mission design, *Johns Hopkins APL Technical Digest (Applied Physics Laboratory)* 1 (2002) 18–33.
- [16] A. F. Cheng, A. S. Rivkin, P. Michel, J. Atchison, O. Barnouin, L. Benner, N. L. Chabot, C. Ernst, E. G. Fahnestock, M. Kueppers, P. Pravec, E. Rainey, D. C. Richardson, A. M. Stickle, C. Thomas, Aida dart asteroid deflection test: Planetary defense and science objectives, *Planetary and Space Science* 157 (2018) 104–115. doi:<https://doi.org/10.1016/j.pss.2018.02.015>.
- [17] D. D. Mazanek, R. G. Merrill, J. R. Brophy, R. P. Mueller, Asteroid Redirect Mission concept: A bold approach for utilizing space resources, *Acta Astronautica* 117 (2015) 163–171. doi:<https://doi.org/10.1016/j.actaastro.2015.06.018>.
- [18] L. Casalino, G. Colasurdo, Missions to Asteroids Using Solar Electric Propulsion, *Acta Astronautica* 50 (1) (2002) 705–711. doi:[https://doi.org/10.1016/S0094-5765\(02\)00006-1](https://doi.org/10.1016/S0094-5765(02)00006-1).
- [19] D. P. S. Santos, A. F. B. A. Prado, L. Casalino, G. Colasurdo, Optimal trajectories towards near-earth-objects using solar electric propulsion (SEP) and gravity assisted maneuver, in: 32° Congresso Nacional de Matemática Aplicada e Computacional, Culabá (Brazil), 2009, pp. 860–866.

- [20] Z. Hasnain, C. A. Lamb, S. D. Ross, Capturing near-Earth asteroids around Earth, *Acta Astronautica* 81 (2) (2012) 523–531. doi:<https://doi.org/10.1016/j.actaastro.2012.07.029>.
- [21] D. Landau, J. Dankanich, N. Strange, et al., Trajectories to Nab a NEA (Near-Earth Asteroid), in: AAS/AIAA Spaceflight Mechanics Meeting, Kauai (HI), 2013, paper AAS 13-409.
- [22] Mascolo, A. D. Iuliis, L. Casalino, Fast and accurate estimation of fuel-optimal trajectories to Near-Earth Asteroids , *Acta Astronautica* 188 (2018) 49–56. doi:<https://doi.org/10.1007/s42064-018-0024-y>.
- [23] N. Strange and E. Asphaug and K. Grogan and others, Planetary Science Decadal Survey - Near-Earth Asteroid Trajectory Opportunities in 2020-2024, Tech. rep., Jet Propulsion Laboratory, California Institute of Technology (2010).
- [24] P. A. Abell, B. W. Barbee, R. G. Mink, et al., The Near-Earth Object Human Spaceflight Accessible Targets Study (NHATS) list of Near-Earth Asteroids: Identifying Potential Targets for Future Exploration, in: *43rd Lunar and Planetary Science Conference*, The Woodlands (The Netherlands), 2012, paper 2842.
- [25] J. P. Sánchez, D. Y. García, Asteroid retrieval missions enabled by invariant manifold dynamics, *Acta Astronautica* 127 (2016) 667–677. doi:<https://doi.org/10.1016/j.actaastro.2016.05.034>.
- [26] A. Jorba, B. Nicolás, Using invariant manifolds to capture an asteroid near the L3 point of the Earth-Moon Bicircular model, *Communications in Nonlinear Science and Numerical Simulation* 102 (2021) 105948. doi:<https://doi.org/10.1016/j.cnsns.2021.105948>.
- [27] E. Fantino, R. Castelli, Efficient design of direct low-energy transfers in multi-moon systems, *Celestial Mechanics & Dynamical Astronomy* 127 (2017) 429–450. doi:<https://doi.org/110.1007/s10569-016-9733>.

- [28] D. Canales, K. C. Howell, E. Fantino, Transfer design between neighborhoods of planetary moons in the circular restricted three-body problem: the moon-to-moon analytical transfer method, *Celestial Mechanics & Dynamical Astronomy* 133 (36) (2021). doi:<https://doi.org/10.1007/s10569-021-10031-x>.
- [29] D. Canales, K. C. Howell, E. Fantino, A versatile moon-to-moon transfer design method for applications involving libration point orbits, *Acta Astronautica* 198 (2022) 388–402. doi:<https://doi.org/10.1016/j.actaastro.2022.06.010>.
- [30] D. Canales, K. C. Howell, E. Fantino, A. J. Gilliam, Transfers between moons with escape and capture patterns via Lyapunov exponent maps, *Journal of Guidance, Control, and Dynamics* 46 (11) (2023) 2133–2149. doi:<https://doi.org/10.2514/1.G007195>.
- [31] G. Donnarumma, Efficient Design of Optimal Low-Energy Trajectories to Near Earth Objects, Master’s thesis, Università degli Studi di Napoli Federico II, Department of Industrial Engineering (2022).
- [32] E. Fantino and G. Donnarumma and M. Grassi, Efficient Design of Optimal of Low-Energy Trajectories to Near Earth Objects, in: 2nd International Stardust Conference (STARCON 2), ESA ESTEC, November 7 - 11, 2022.
- [33] D. Canales, E. Fantino, K. C. Howell, R. Flores, Design of optimal spatial low-energy trajectories to Near Earth Objects, in: 74th International Astronautical Congress, Baku (Azerbaijan), 2023, paper IAC-23-C1.6.1.
- [34] NASA Jet Propulsion Laboratory, Astrodynamics parameters, <https://ssd.jpl.nasa.gov/astro-par.html>, (last accessed 25 Aug. 2023).
- [35] T. S. Parker, L. Chua, Practical numerical algorithms for chaotic systems, Springer-Verlag, New York, 1989.

- [36] NASA Jet Propulsion Laboratory, Small bodies database query, https://ssd.jpl.nasa.gov/tools/sbdb_query.html, (last accessed 25 Aug. 2023).
- [37] W. L. S. Wen, A study of cotangential, elliptical transfer orbits in space flight, *Journal of Aerospace Sciences* 28 (5) (1961) 411–417. doi:<https://doi.org/10.2514/8.9010>.